

See discussions, stats, and author profiles for this publication at: <https://www.researchgate.net/publication/228634057>

Deformation-Induced Phase Transition and Superstructure Formation in Poly(ethylene terephthalate)

ARTICLE *in* PHYSICAL REVIEW. E, STATISTICAL PHYSICS, PLASMAS, FLUIDS, AND RELATED INTERDISCIPLINARY TOPICS · DECEMBER 2004

Impact Factor: 2.81 · DOI: 10.1021/ma049333x

CITATIONS

67

READS

60

9 AUTHORS, INCLUDING:



Benjamin S Hsiao

Stony Brook University

571 PUBLICATIONS 20,554 CITATIONS

SEE PROFILE



Shaofeng Ran

32 PUBLICATIONS 2,175 CITATIONS

SEE PROFILE



Takeshi Kikutani

Tokyo Institute of Technology

170 PUBLICATIONS 1,324 CITATIONS

SEE PROFILE



Benjamin Chu

Stony Brook University

677 PUBLICATIONS 21,083 CITATIONS

SEE PROFILE

Deformation-Induced Phase Transition and Superstructure Formation in Poly(ethylene terephthalate)

Daisuke Kawakami,[†] Benjamin S. Hsiao,^{*,†} Christian Burger,[†] Shaofeng Ran,[†] Carlos Avila-Orta,[†] Igors Sics,[†] Takeshi Kikutani,[‡] Karl I. Jacob,[§] and Benjamin Chu[†]

Department of Chemistry, State University of New York at Stony Brook, Stony Brook, New York 11794-3400, Department of Organic and Polymeric Materials, Tokyo Institute of Technology, O-okayama, Meguro-ku, Tokyo 152, Japan, and School of Polymer, Textile & Fiber Engineering, Georgia Institute of Technology, 801 Ferst Drive, Atlanta, Georgia 30332-0295

Received April 5, 2004; Revised Manuscript Received October 24, 2004

ABSTRACT: Deformation-induced phase transitions and superstructure formation in poly(ethylene terephthalate) (PET) were studied by means of in-situ synchrotron small-angle X-ray scattering (SAXS) and wide-angle X-ray diffraction (WAXD) as well as Raman spectroscopy. The deformation conditions involved uniaxial stretching of quenched PET films at a temperature just below its glass transition temperature (T_g), where a notable “plastic deformation” stage was observed. WAXD results indicated that the initial sample contained a “slush” structure (amorphous + nematic), whereby deformation induced oriented amorphous, nematic, smectic (C and quasi-A), and stable triclinic crystalline phases. SAXS results indicated that the fibrillar superstructure was formed upon the formation of oriented slush. In-situ Raman spectroscopic data revealed the orientation information on ethylene glycol and benzene ring as well as the *gauche*–*trans* transition in deformation of PET chains, which are in good agreement with X-ray results. A mechanism for deformation-induced phase transitions and for hierarchical structure formation has been proposed to correlate the structural information with the mechanical properties.

1. Introduction

The recent simulation work by Frenkel et al.¹ indicated that the isotropic–nematic transition occurs when the aspect ratio of the mesogenic molecule (L/D , where L represents the length and D represents the diameter) is in the range of 3–4. In view of poly(ethylene terephthalate) (PET), its persistence length is about 1.33 nm, and the average molecular diameter is about 0.66 nm based on the experimental work by Imai et al.² This suggests that the aspect ratio of the PET mesogenic unit is around 2, which falls short of being a liquid crystalline polymer. However, the existence of mesomorphic phases has been well documented in oriented PET samples. Bonart was the first to report the formation of nematic and smectic phases during the tensile stretching of PET using the conventional X-ray diffraction method.^{3,4} Recently, with the use of high-intensity synchrotron X-rays, more detailed features of mesomorphic phases in oriented PET have been revealed by different research groups. For example, Windle et al. reported the formation of a transient smectic phase in oriented fibers made of random PET and PEN (polyethylene naphthalene-2,6-dicarboxylate) copolymers.^{5,6} Asano et al. reported the appearance of smectic order at 60 °C having a spacing of 1.07 nm during the annealing of cold-drawn amorphous PET films.⁷ Blundell and co-workers observed the smectic A structure during the fast extension of PET. They proposed that the smectic structure is a precursor of the crystalline structure based on the simultaneous appearance of the triclinic crystalline peak

and disappearance of the smectic peak.^{6,8–12} Hsiao and co-workers reported the smectic C phase during the deformation of amorphous PET film below the glass transition temperature (T_g) at 50 °C.¹³ They observed that the mesophase developed immediately upon the neck formation. As the mesophase contained a sharp meridional peak 001' ($d = 1.032$ nm), which was smaller than the monomer length in the typical triclinic unit cell ($c = 1.075$ nm), they concluded that the chains in the mesophase formed an inclined smectic C structure.

Thus, PET may be considered as a “marginal” liquid crystalline polymer. Its mesomorphic transitions are not obvious in the unoriented (isotropic) state but are distinct in the oriented state. In a way, the kinetic pathways of the phase transition in PET may be too long to be observed under the isotropic conditions, while the deformation process can overcome the kinetics barrier and reveal all possible transitions. It is conceivable that the varying mesomorphic phases reported in the earlier studies are simply due to the different experimental conditions involved, where all mesomorphic structures (e.g., oriented amorphous, nematic, smectic C, and quasi-smectic A) can be induced by stretching. In the present study, our first objective was to construct a deformation-induced phase transition mechanism for PET, using an amorphous sample as the starting phase at a suitable temperature where all the reported mesomorphic phases can coexist.

The second objective of this study was to correlate the phase transition with the superstructure formation in PET under uniaxial deformation, which was prompted by two recent studies. Asano et al. observed that the smectic A structure (observed by WAXD, with the characteristic meridional d spacing = 1.07 nm) was related to the occurrence of lamellar layer structure having a 10 nm repeat spacing (by SAXS) during the

[†] State University of New York at Stony Brook.

[‡] Tokyo Institute of Technology.

[§] Georgia Institute of Technology.

* To whom correspondence should be addressed: Tel 631-632-7793; Fax 631-632-6518; e-mail bhsiao@notes.cc.sunysb.edu.

annealing of cold drawn PET film.⁷ Mahendrasingam et al. reported that there was a strong relationship between the smectic mesophase (WAXD) and the fibrillar superstructure associated with the equatorial scatter (SAXS).¹⁴ It is clear that there is a distinct correlation between the superstructure formation (e.g., fibril and lamellae) and the phase transition; however, the correlation is not completely clear at the current state, but it can be resolved by the use of combined in-situ SAXS and WAXD techniques.

Finally, the present study was conducted to understand the mechanical properties and the structure/mesophase relationships. Recently, our group has investigated the mechanism of structural formation and its relationship with the stress-strain curves in amorphous PET above its T_g (90 °C).^{15,16} Results indicated that the structural development can be categorized into three zones, designated I, II, and III. In zone I, the oriented mesophase is induced by strain, where the applied load remains about constant (this is typically termed the “plastic deformation” stage in PET). In zone II, crystallization is initiated from the oriented mesophase through nucleation and growth, where the load starts to increase marking the beginning of the strain-hardening region. In zone III, the stable crystal growth process is facilitated by strain-induced orientation until the breaking of the sample, where the ratio between load and strain remains about constant. We are particularly interested in the process of plastic deformation, in which the strain increases without any significant increase in stress. It has been argued that displacements of atoms related to slip and yielding require “free volume”, which increases in tension, making it easier for polymers to yield under tensile stresses.¹⁷ It is conceivable that the yield plateau is closely related to the phase transition and the structure formation.

To address the above issues, we have carried out in-situ SAXS and WAXD measurements in PET samples under tensile deformation. The sample temperature was kept at 70 °C, below its T_g , to reveal all mesomorphic phases by reducing the rates of phase transitions and to maintain a notable “plastic deformation” stage. On the basis of our previous studies, we noticed that if the deformation temperature was high (e.g., above T_g at 90 °C), no smectic phase could be observed;^{15,16} while if the deformation temperature was low (below T_g at 50 °C), the “plastic deformation” stage was relatively narrow.¹³ In addition, we have adopted in-situ Raman spectroscopy measurements to obtain molecular information on PET chains during deformation, which complemented the results from WAXD and SAXS studies.

2. Experimental Section

2.1. Samples Preparation. The PET sample (in the pellet form) was specially prepared by Toray Co. Ltd. in Japan for this study. The weight-average molecular weight (M_w) of this PET sample was 35 000 g/mol, and the polydispersity was around 2.0. Minimum amounts of antimony (the catalysis for polymerization) and phosphate (the additive to enhance the heat durability) were used to prepare this sample. Thus, the sample could be viewed as pure polymer that would not decompose under high molding temperatures. No other additives for copolymerization and plasticization were used. The PET sample was dried in a vacuum oven at 150 °C for 6 h and was subsequently crystallized at 120 °C for 3 h in air. The sample was subsequently molded into dog-bone-shaped samples (see Figure 1) at 270 °C followed by rapid quenching with ice water (0 °C). The length of the dog-bone sample that can be drawn was 25 mm including the taper part, with 6 mm

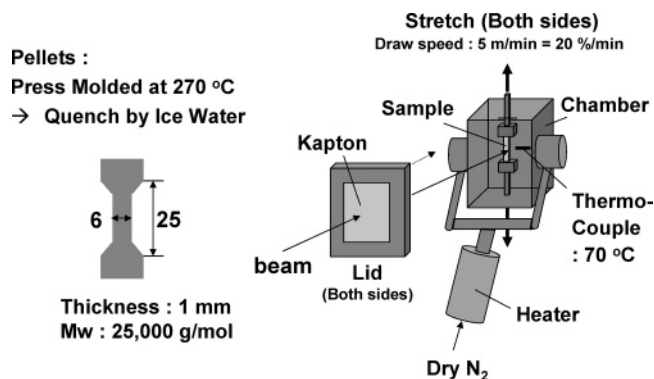


Figure 1. Sample of dog-bone-shaped (left) and experimental setup of heating and drawing chamber for in-situ SAXS/WAXD study (right).

in width and 1 mm thickness. A small notch was incorporated at the central point of the dog-bone sample in order to initiate and stabilize the onset of necking. The final weight-average molecular weight (M_w) of the molded samples was about 25 000 g/mol. The decrease in the molecular weight was due to the process of hydrolysis in the atmosphere during molding instead of thermal decomposition. The molded samples were completely amorphous, having no detectable crystallinity (by X-ray and DSC).

2.2. Experimental Procedures. The experimental setup for the in-situ drawing study is shown in Figure 1. The sample was mounted in an environmental chamber, which was heated by dry hot nitrogen, for the deformation studies with X-ray and Raman. The dog-bone sample was equilibrated in the chamber for 3 min after being heated to the desirable temperature (70 °C), before subjecting the sample to any tensile deformation. The chosen deformation rate was 20%/min. The deformation process was continued until the sample broke. The load-strain curve was recorded simultaneously during the collection of the WAXD, SAXS, and Raman signals. Another sample of the same molecular weight was also used to collect X-ray and Raman data in a heat chamber at 70 °C without deformation for 40 min, which was used as a referenced state; i.e., the averaged WAXD image was used as the reference for the amorphous phase. No crystallization was observed in the samples before and after the thermal treatments at 70 °C.

2.3. Synchrotron X-ray Measurements. Synchrotron X-ray measurements were carried out at the X3A2 Beamline in the National Synchrotron Light Source (NSLS), Brookhaven National Laboratory (BNL). The wavelength of this beamline was 1.54 Å. A three-pinhole collimator system was used to reduce the beam size to 0.6 mm in diameter.¹⁸ A modified Instron 4410 was used in the stretching study, which allowed symmetrical stretching, where the focused X-ray beam always illuminated the same position on the film during deformation. The engineering deformation rate (i.e., the cross-head speed) was kept constant at 5 mm/min (i.e., 20% strain/min), and the sample temperature was maintained at 70 °C. (The true strain was not always the same as the applied strain because of sample necking.) The collection time for 2D WAXD image was 20 s, and that for 2D SAXS was 60 s using a CCD X-ray detector (MAR). The sample-to-detector distance was 118 mm for WAXD and 1407 mm for SAXS. The diffraction angle in WAXD was calibrated by using a polypropylene standard and an Al₂O₃ standard (from the National Institute of Standards and Technology, NIST). The scattering angle in SAXS was calibrated by an AgBe standard. The high intensity of synchrotron X-rays made it possible to collect the WAXD and SAXS patterns during stretching in real time without holding.

2.4. Raman Measurements. Polarized Raman spectra were recorded in real time by a Renishaw RM series 1000B. The spectrometer was controlled by the WiRE software provided by Renishaw, and the collected data were analyzed by the Grams32 software (Galactic Industries Corp.). The laser (wavelength 785 nm) was introduced into the spectrometer via optical fibers. The remote probe, consisting of a cylindrical

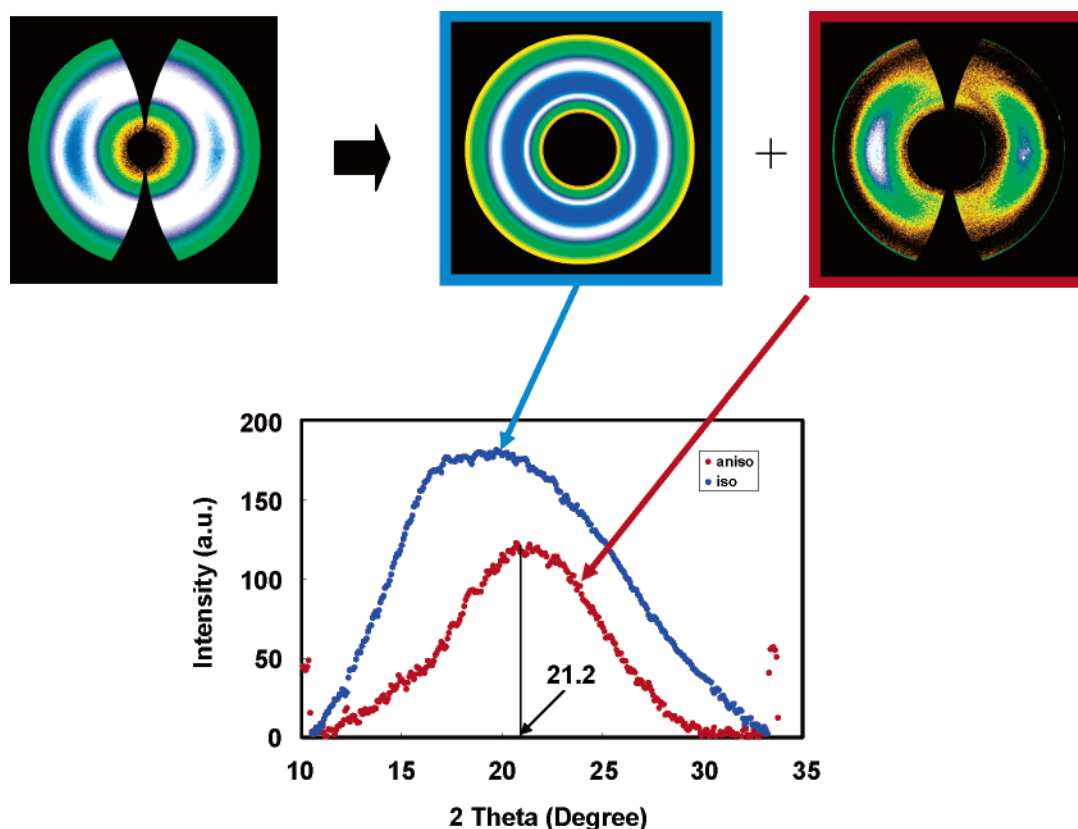


Figure 2. Example separation of Fraser-corrected 2D WAXD pattern (collected at 25% strain) into isotropic and oriented fractions (top). Linear intensity profiles taken from the equatorial scans of separated isotropic and oriented patterns (bottom).

head, condensed eyeglass, polarizer, and optical fiber, was used to illuminate the sample. This probe unit was mounted on an XY stage, which was controlled remotely by using stepping motors so that the focal point of the laser could remain at the same position on the sample. The reflected signals were transmitted back to the spectrometer by the eyeglass, analyzer, and optical fiber. The data collection time for each spectrum was 1 min, and the spectrum range was 500–2000 cm^{-1} .

Samples for in-situ Raman measurement, prepared under the exactly the same conditions as for X-ray measurements, were carefully mounted in the environmental chamber of the modified Instron 4410 apparatus (Figure 1). The deformation rate and the sample temperature for the Raman study were the same as for the X-ray study, which were 5 mm/min (i.e., 20% strain/min) and 70 °C, respectively. A silicon wafer was used as the standard sample to calibrate the wavenumber as well as to adjust the resolution, scan number, and laser power.

2.5. WAXD Data Analysis. All two-dimensional (2D) WAXD patterns were corrected by the Fraser method¹⁹ to compensate the detection by a flat-plate detector (Mar CCD). The Fraser corrected image was then separated into two parts: isotropic (unoriented) and anisotropic (oriented) fractions, using an image analysis method described elsewhere.¹³ The example separation procedure for a WAXD pattern collected at the initial stage of deformation (applied strain = 25%) is illustrated in Figure 2. The amount of the oriented fraction was assumed to be proportional to the total area from the separated anisotropic pattern, whereas the amount of the isotropic fraction was assumed to be proportional to the separated isotropic pattern.

At higher strains, the WAXD image can exhibit a pair of (001') reflections on the meridian, indicating the presence of the smectic phase. The fraction of the smectic phase was estimated by the following procedure. The integrated diffraction intensity profile was obtained from the Fraser corrected 2D WAXD image with meridional extrapolation into the "missing region" using a Legendre expansion.¹³ The area of the fitted (001') peak from the 1D profile was used to determine the mass fraction of the smectic phase (i.e., the (001') area

divided by the total diffraction intensity profile). The mass fraction of the oriented slush (amorphous + nematic) was obtained by subtracting the smectic fraction from the total oriented mesomorphic fraction determined above. The d spacing of the smectic phase was also estimated by the deconvoluted (001') peak from the 1D profile.

The crystalline sizes along different directions were determined directly from the equatorial and meridional slices of the 2D WAXD pattern (without Fraser correction). In the WAXD image collected at high strains, three crystalline peaks ((010), (-110), (100)) and one slush background peak were identified in the equatorial profile; one (001') smectic peak, one (103) crystalline peak, and two slush peaks (oriented and unoriented) were identified in the meridional profile. Each peak was fitted by a mixed function of Gaussian and Lorentzian (eq 1) by use of a peak-fitting program (Grams 32 software).

$$f_{\text{MIX}} = (1 - M)(\text{Gaussian}) + M(\text{Lorentzian}) \quad (1)$$

where M is the weight fraction of the Lorentzian function.

The position and the full width at half-height (fwhh) of the fitted crystalline peak were used to determine the d spacing (using the Bragg's law) and the crystal size (using the Scherrer equation), respectively. The Scherrer equation can be expressed as follows²⁰

$$D_{hkl} = K\lambda/(\beta_{1/2} \cos \theta) \quad (2)$$

where D_{hkl} represents the apparent lateral crystallite size of the hkl reflection plane, $\beta_{1/2}$ is the fwhh of the diffraction peak hkl in radians, the shape factor K is set at 0.9 for polymer systems, λ is the X-ray wavelength, and θ is half of the diffraction angle. We recognize that there is the possibility of lattice distortion due to the broadening of the line width, leading to an underestimation of the crystal size. However, this possibility could not be estimated due to the lack of suitable higher order reflections for evaluation. According to Salem,^{21,22} the contribution of the lattice distortion is likely to

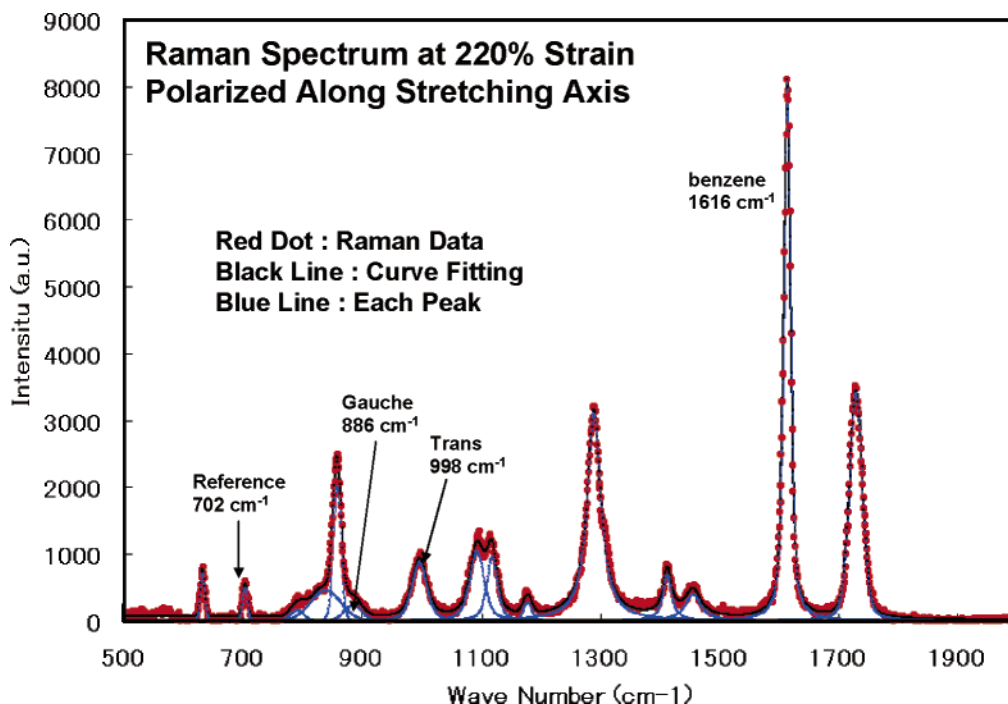


Figure 3. Example of peak deconvolution of the Raman data collected during deformation at an applied strain of 220%.

be small. Strictly speaking, the analysis by inverse integral peak width should be used to determine the crystalline size. However, the Scherrer equation is used in this study to estimate crystal size since it has been widely used in many previous studies.

2.6. Raman Data Analysis. The *trans* and *gauche* conformer change and molecular orientation in PET chains during deformation were extracted from the Raman spectroscopic data. The Grams 32 software was again used to deconvolute all vibrational peaks in the spectrum. Each peak was fitted by a mixed function of Gaussian and Lorentzian as shown in eq 1. Typical peak fitting results (e.g., *trans* and *gauche* conformational peaks and the benzene peak) of the Raman spectrum measured during deformation of a PET dog-bone sample is given in Figure 3.

2.6.1. *Trans*–*Gauche* Content. In Figure 3, the peak at 998 cm^{−1} is assigned as the *trans* conformation of the ethylene glycol (EG) fragment either in the isotropic, mesomorphic, or crystalline regions, where the peak at 886 cm^{−1} is assigned as the vibration of the *gauche* conformer of the same fragment.^{23–27} For quantitative purpose, the band at 702 cm^{−1} can be considered as an internal reference band.^{23–25} As the technique involving polarization^{28–32} was used in this study, the total amount of each peak can be estimated by the following formula:²⁹

$$\begin{aligned} A_{\text{parallel}}(\nu) &= I_{\text{parallel}}(\nu)/I_{\text{parallel}}(\text{ref } \nu) \\ A_{\text{vertical}}(\nu) &= I_{\text{vertical}}(\nu)/I_{\text{vertical}}(\text{ref } \nu) \\ A(\nu) &= A_{\text{parallel}}(\nu) + 2A_{\text{vertical}}(\nu) \end{aligned} \quad (3)$$

where $I_{\text{parallel}}(\nu)$ and $I_{\text{vertical}}(\nu)$ represent the peak areas at wavenumbers ν cm^{−1} taken by polarized laser light parallel and vertical to the tensile direction, respectively ($I_{\text{parallel}}(\nu)$ and $I_{\text{vertical}}(\nu)$ are often termed the ZZ and ZX spectra, where Z represents the stretching axis, ZZ indicates that both polarizer and analyzer are parallel to the stretching axis, and ZX indicates that the polarizer is set parallel to the stretching axis and the analyzer is set perpendicular to the stretching). After the values of $A(\nu)$ at 998 and 886 cm^{−1} at each strain were calculated, they were fitted to the following expression using the least-squares method^{26,27}

$$p_1 A(998) + p_2 A(886) = 1 \quad (4)$$

where p_1 and p_2 represent the fitting coefficients, which were estimated to be 0.311 and 0.321, respectively.

2.6.2. Molecular Orientation. One important aspect of the polarized Raman spectroscopy is that using this technique it is possible to extract the orientation of each molecular segment including benzene ring, ethylene glycol, and so forth. The orientation of the segment can be estimated by dichroic function (DF) as expressed as follows:²⁹

$$\text{DF}(\nu) = (A_{\text{parallel}}(\nu) - A_{\text{vertical}}(\nu))/(A_{\text{parallel}}(\nu) + 2A_{\text{vertical}}(\nu)) \quad (5)$$

In this study, the DF values for two peaks at 998 and 1616 cm^{−1} were estimated, which represent the orientation of the *trans* glycol conformer and the benzene frame, respectively. Strictly speaking, five spectra are necessary to determine five unknowns, which would consist of three Raman tensor components as well as two orientation components P_2 and P_4 (or second- and fourth-rank order parameters ($\langle P_2(\cos \theta) \rangle$ and $\langle P_4(\cos \theta) \rangle$). For example, Lesco et al. have measured all five spectra to determine the orientation of the 1616 cm^{−1} peak,³³ and Yang et al. have also done a similar analysis for the 998 cm^{−1} peak.^{24,25} However, for simplicity, we have carried out the analysis using only two spectra ($I_{\text{parallel}}(\nu)$ and $I_{\text{vertical}}(\nu)$). As both 998 and 1616 cm^{−1} peaks have very strong anisotropy under polarization measurements, the trend of the change in orientation for each component estimated using the simplified method is sufficient to compare with the X-ray results.

3. Results and Discussion

From our earlier deformation study of an amorphous PET film below and above T_g (at 50 and 90 °C, respectively)^{13,15,16} and the cursory evaluation of 2D WAXD images through both face-on and edge-on directions in the present study, we observed that the structure developed from the deformed amorphous sample had a cylindrical symmetry. This assumption significantly simplified the data analysis schemes.

3.1. Deformation-Induced “Phases” in PET. As the purpose of this study was to elucidate the phase transition in PET, induced by uniaxial deformation, the term “phase” was used not from the thermodynamic standpoint but from the structure standpoint based on

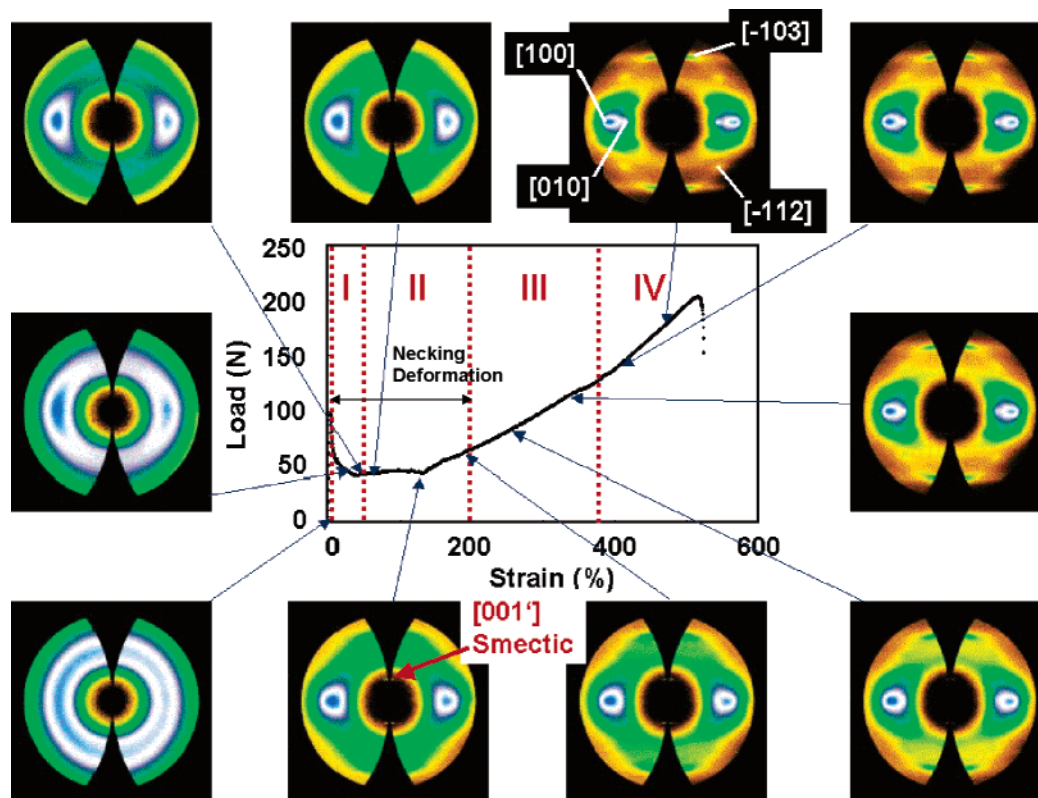


Figure 4. Selected WAXD images (normalized with the Fraser correction¹⁹) during the collection of load–strain curve at 70 °C.

WAXD observations. The assigned “phases” in this study are as follows.

(1) “*Isotropic Slush*”. The reason we choose the word “slush” to describe the initial structure of unoriented quenched PET sample is because we do not know whether the initial sample is completely amorphous, nematic, or having mixed amorphous/nematic phases. Although the nematic phase in PET has never been fully verified, its likely existence in the quenched sample has been clearly pointed out by Geil et al. in a TEM study.³⁴ On the basis of this consideration as well as the structure transition results to be presented later, we feel it is more reasonable to assign the initial sample with an isotropic “slush” structure, containing both isotropic amorphous and nematic phases rather than a pure isotropic amorphous phase. The scattering features from the isotropic amorphous phase, the nematic phase without preferred domain orientation, and the slush phases are similar, all exhibiting an isotropic scattering halo in the 2D WAXD image.

(2) “*Oriented Slush*”. Upon deformation, the 2D WAXD pattern exhibited two broad scattering peaks on the equator centered on the origin. No other diffraction peak was observed. This scattering feature could be attributed to the oriented shish structure, consisting of oriented amorphous phase and nematic phase with preferred domain orientation. As shown in Figure 2, the equatorial intensity profile from the anisotropic fraction exhibited a narrower peak with the center located at a higher angle than that of the isotropic fraction. Thus, the oriented structure (concentrated on the equator) should contain higher density and more homogeneous arrangement than the isotropic structure.

(3) “*Oriented Smectic Phase*”. The unique scattering feature of the oriented smectic phase is the presence of (001′) reflection peak on the meridian, which corresponds to a ca. 1 nm layered structure.

(4) “*Oriented Crystalline Phase*”. Upon crystallization, the 2D WAXD pattern exhibits multiple reflections typical of a PET triclinic unit cell. The cell parameters, however, are functions of the deformation strain.

3.2. Categorization of Structure Evolution in the Stress–Strain Curve. On the basis of our prior in-situ WAXD study,^{15,16} the load and strain curve measured at 70 °C can be divided into four zones (I–IV) to facilitate the discussion. These zones can be categorized on the basis of the characteristics of the deformation-induced phases. Figure 4 shows the load–strain (applied stress–strain) curve in conjunction with selected WAXD images that have been corrected by the Fraser method (i.e., these images are illustrated in undistorted reciprocal space).¹³

In zone I (0–55%), the sample was found to deform homogeneously prior to the yield point (15% strain). But before the yield point, there was no orientation in WAXD (this was also confirmed in the edge-on view). Only at strains above 15%, necking was observed and scattering orientation in WAXD was seen. Usually, if the PET sample is stretched near room temperature (even at 50 °C¹³), distinct neck formation occurs. However, the neck formation at 70 °C was found to be zonelike rather than linelike. The length of the neck zone was 3–4 mm. The necking was started near the center of the sample, where a small notch was initially implemented. The majority of zone I thus corresponded to the initiation of a “neck zone” near the illuminating point. (The neck formation lasted until 200% of applied strain, whereas the applied stress began to develop at about 130% strain.) As the initial sample thickness was less than 1 mm, the uncertainty of the true strain determined in the neck zone was relatively large ($\pm 10\%$). With the assistance of a sample monitoring device using video camera, we estimated that the applied strain from 15 to 55% corresponded to a true

strain range from 15 to 200% and that the applied strain ratio of 20% strain/min corresponded to the true strain ratio of 90–95% strain/min. In view of the large uncertainty in the true stress–strain relationship, only applied stress–strain relationships will be discussed hereafter.

In Figure 4, a singular equatorial scattering peak appeared after the yield point in zone I, where no other scattering feature occurred. This scattering feature can be attributed to the formation of oriented slush (a mixture of oriented amorphous and nematic phases). Zone I thus represents the transformation from the isotropic slush to the oriented slush by deformation. At strains above 55%, a distinct (001') peak on the meridian appeared in WAXD (Figure 4), which is the characteristics of the oriented smectic phase in PET and marks the beginning of zone II (applied strain 55–200%). The increase of the (001') intensity indicates that the population of the smectic phase increases in zone II. In zone III (applied strain 200–370%), the applied stress developed nearly linearly with applied strain. Stain hardening was found to occur in both zones III and IV until the sample broke. In zone III, the equatorial (010) reflection appeared, which is indicative of the occurrence of the triclinic crystalline phase. Thus, the main feature in zone III is the transition of oriented crystalline phase from the oriented smectic phase. The final stage is zone IV (applied strain 370–500%), where the development of oriented crystalline phase becomes dominant but at a relatively slower rate. The detailed relationships among the phase transitions, superstructure formation (determined by SAXS), and mechanical response in each zone are described as follows.

3.3. Zone I: Induction of Oriented Slush and Formation of Fibrillar Superstructure. The major scattering feature in this zone is the appearance of singular oriented scattering peak on each side of the equator, where the intensity and orientation of the scattering peak all increase with applied strain (Figure 4). The linear intensity profiles taken along the equator and the meridian are illustrated in parts A and B of Figure 5, respectively, and the azimuthal intensity profiles integrated from $s = 1$ –4 are illustrated in Figure 5C (azimuthal angle = 0° represents the meridional axis, azimuthal angle = 90° represents the equatorial axis).

In Figure 5A,B, it is seen that in zone I the position of the equatorial scattering peak remains about constant and its integrated intensity increases with strain, whereas the position of the meridional scattering peak is shifted to a lower scattering angle and its integrated intensity decreases with strain. Judging by the shape of the original peak (i.e., the initial curves of the equatorial profile or the meridional profile at 0% strain, which are the same) and the change of the curve shape with applied strain (Figure 5A,B), the lower-angle scattering portion appeared to remain constant under deformation, while the higher-angle portion changed strongly with applied strain in the meridian profile. At higher strains, the high-angle portion aggregates near the equator, which was primarily responsible for the total scattering changes in zone I. In Figure 5C, the azimuthal profiles in zone I illustrate an increase in molecular orientation with applied strain.

As stated earlier, we do not know whether the initial PET sample was completely amorphous or had mixed amorphous and nematic phases. The existence of the

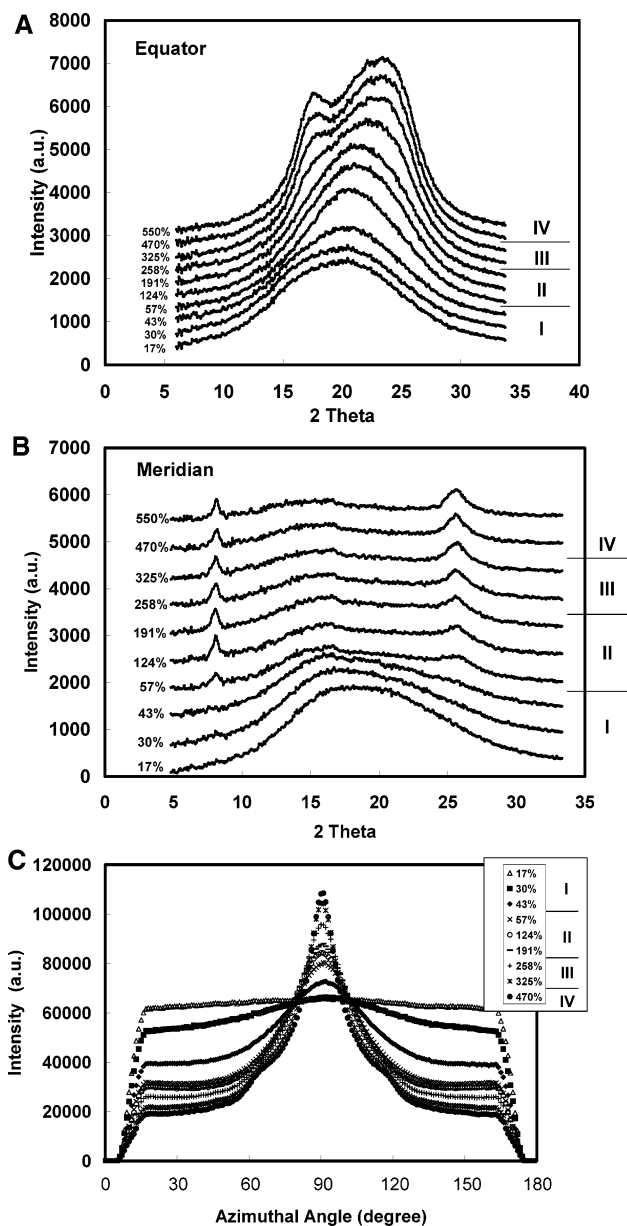


Figure 5. Linear diffraction intensity collected from (A) equatorial scans, (B) meridional scans, and (C) azimuthal profiles (integrated from $s = 1$ to $s = 4 \text{ nm}^{-1}$) of the 2D WAXD images illustrated in Figure 4.

nematic phase in quenched PET, although never directly verified, has been frequently cited. For example, in addition to the work by Geil et al.,^{34,36,37} the recent simulation study carried out by Taiko et al. indicated that the weak dipole–dipole interactions in PET, making the coexistence of amorphous and nematic phases likely.³⁸ Kimura et al. demonstrated the magnetic orientation in PET chains, which is consistent with the characteristics of liquid crystalline polymer.³⁹ The oriented nematic structure in PET has also been suggested in some deformation studies. Asano et al. compared the WAXD data and the density (1.37 g/cm^3) of the cold drawn PET sample and concluded that a significant fraction of molecules is aligned nearly parallel to the draw direction. They assumed these molecules adopted a nematic structure.⁷ With WAXD and SAXS measurements, Fukao et al. proposed a kinetic model from nematic to smectic phases in PET.³⁵ On the basis of these studies as well as our own observations, we also postulate the possible existence of nematic phase in

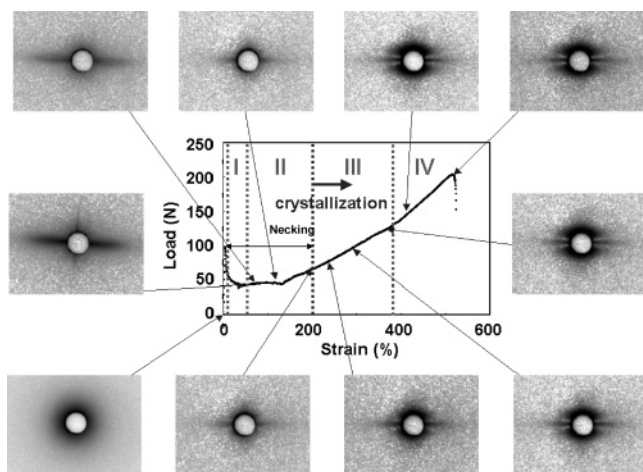


Figure 6. Selected SAXS images during the collection of load-strain curve at 70 °C.

quenched PET sample. It is conceivable that the high-angle portion of the WAXD profile in the initial sample composed of a nematic dominant structure because it would have higher density. This hypothesis is certainly consistent with the linear intensity profiles, extracted from the equatorial scans of unoriented and oriented fractions of slightly deformed PET (strain = 25%) in Figure 2. In this figure, the intensity profile from the anisotropic fraction exhibited a narrow peak with its center located at a larger angle (21.2°) than that from the isotropic fraction. Thus, the oriented fraction should have a denser and more homogeneous molecular structure, such as the nematic phase, than the isotropic fraction, such as the amorphous phase. We assumed that the initially unoriented and oriented “slush” structure contained both amorphous and nematic phases.

Figure 6 shows selected SAXS images collected during in-situ deformation at 70 °C at various strain levels. Although only two images were shown in zone I (including the first image from the original sample), it was interesting to note that a strong equatorial streak appeared immediately after the yield point. (The second SAXS image corresponds to the accumulation during 20–40% applied strain.) The streak image was drastically different from the SAXS image of the undeformed sample, where only diffuse scattering was seen. The equatorial streak may be attributed to two possibilities: (1) the formation of microvoids (crazes)^{40,41} and (2) the formation of fibrillar superstructure.^{42–45} Judging by the relatively weak scattered intensity (the void scattering usually gives strong intensity) and the transparent appearance of the deformed sample (observed by the sample monitoring camera), we conclude that this equatorial streak in SAXS is mainly due to the formation of fibrillar superstructure, which have been observed in both solid polymers under extensional strains^{44–46} and molten samples under shear.^{47,48} The length of the fibrillar superstructure was found to be in the range of several hundred nanometers, and the diameter is in the range of tens of nanometers by using the method developed by Grubb et al.^{42,43} On the basis of the simultaneous appearance of the oriented slush (in large fraction, which will be discussed next) and the formation of fibrillar superstructure, we speculate that these two events probably take place in a coupled manner; i.e., the superstructure of the oriented slush is fibrillar-like.

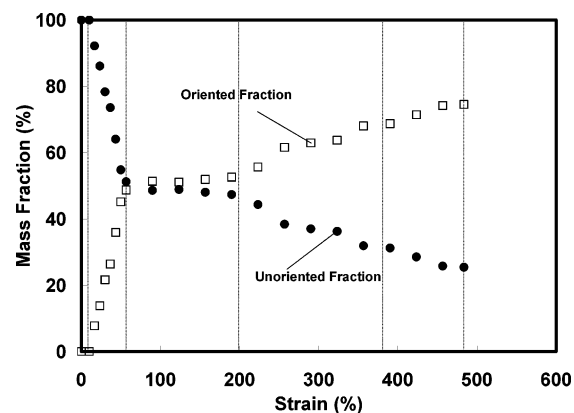


Figure 7. Mass fractions of isotropic and oriented fractions extracted from 2D WAXD patterns during uniaxial deformation.

To quantify the phase behavior, the mass fractions of unoriented and oriented slush were estimated by using the analytical procedures outlined in the Experimental Section. Results are shown in Figure 7. In this figure, the following “phases” were assumed in each fraction: (1) isotropic fraction containing amorphous and nematic phases; (2) oriented fraction containing amorphous, nematic, smectic, and crystal phases. In zone I, the oriented fraction did not include the smectic phase and was found to increase quite substantially with applied strain. (However, it reaches a plateau value at about 55% strain.) The formation of the oriented fraction was directly related to the disappearance of the isotropic fraction.

In zone I, the relationship between the structure and the mechanical behavior is quite interesting. The sample was found to deform quite homogeneously before the yield point (15% strain). However, no orientation in WAXD and no scattering feature in SAXS were seen in this stage. Upon further deformation, the load decreases from the yield point and reach a lower plateau value. The yield stress thus reflects the energy necessary to overcome the initial formation of oriented slush from isotropic slush and is probably related to the energy barrier for the orientation of nematic domain in the slush.

3.4. Zone II: Transition from Oriented Slush to Oriented Smectic Phase in Fibrillar Superstructure. Zone II is dominated by two features: (1) the appearance of a large “plastic deformation” stage, where the applied load is the lowest but is about constant, and (2) the appearance of oriented slush (nematic)–smectic transition (Figures 5B and 8). The two processes are necessarily related to each other.

From the microscopic perspective, the process of plastic deformation can be described as follows. When the engineering stress, normalized with the initial cross-sectional area, is plotted against the engineering strain, an elastic limit is reached. At strains above the elastic limit (typically at a very low strain), permanent deformations remain even after complete unloading. Typical polymer solids usually show a large yield plateau at high engineering strains. The simplest approximation for this yield plateau in the theory of plasticity is an “ideal” plastic behavior, in which the strain increases without any increase in stress. Beyond the yield plateau, strain hardening occurs, where the material stiffens resulting from increased modulus. The basic expressions to describe the plastic flow are similar to the equations

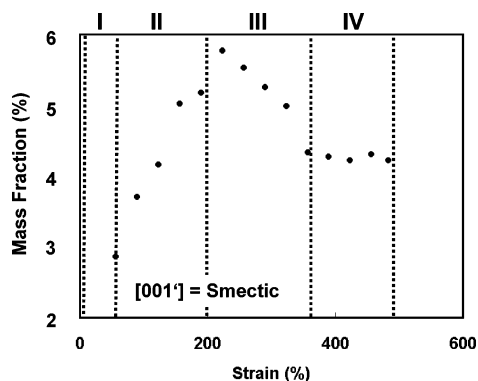


Figure 8. Mass fractions of the smectic phase by WAXD during deformation at 70 °C.

to describe the flow of a viscous fluid.^{49–51} Yielding and plastic deformation is essentially a viscous flow process satisfying kinetic relationships similar to liquids. Like flow of incompressible liquids, plastic flow usually takes place with constant volume. Thus, the deformation associated with the yield plateau is considered as a plastic flow. However, it should be noted that time is not a necessary parameter to represent plastic flow, while time is essential to characterize viscous flow.

In zone II, if we assume that the change of the sample density in PET is relatively small during deformation, then the stress at the neck zone should remain about constant since the corresponding applied load and the cross-section area are nearly unchanged. (The stress of the unnecked part was estimated to be 22 MPa, whereas that of the necked part was estimated to be 21 MPa in this zone.) This condition will meet the requirement of plastic deformation. It is interesting to note that although the total mass fraction of the oriented mesophase (the oriented slush plus the oriented smectic phase) remains about constant during the plastic deformation stage (Figure 7), the mass fraction of the smectic phase is found to increase in zone II (Figure 8). This suggests that the conversion of oriented slush (nematic) to smectic phase is not related to the applied stress gradients but may be attributed to the annealing effect at 70 °C. In other words, the plastic deformation is probably mainly due to the orientation “flow” of the slush phase, where the nematic–smectic transition is due to the annealing effect.

On the basis of the intensity of the (001') reflection, the mass fraction of the oriented smectic phase was estimated, and the results are shown in Figure 8. It was seen that the mass fraction of smectic phase increased almost linearly with applied strain in zone II, whereas the total oriented fraction remained about constant (Figure 7). This suggests that the transition from oriented slush (nematic) to smectic phase occurs mainly in the oriented slush domain, i.e., within the fibrillar superstructure. The fibrillar structure is found to be stable in zone II (Figure 6), as indicated by the persistent appearance of the equatorial streak feature in SAXS. In Figure 6, the first SAXS image collected in zone II exhibited a stronger equatorial streak pattern than the rest of the images in zone II. This is because the first image included some scattering contribution from the structure in zone I. The rest images in zone II showed very similar equatorial streak pattern with relatively weaker intensity. Asano et al. reported that the nematic structure is the precursor of smectic structure, and our data support this hypothesis.⁷

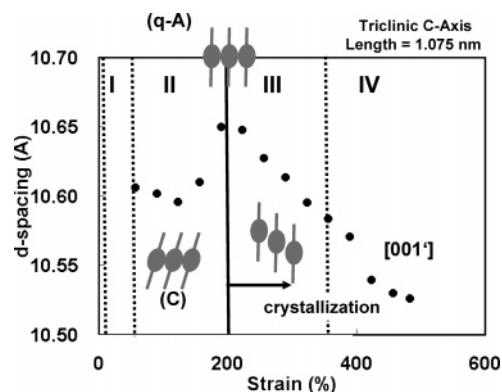


Figure 9. Change of d spacing of (001') peak by WAXD during uniaxial deformation at 70 °C.

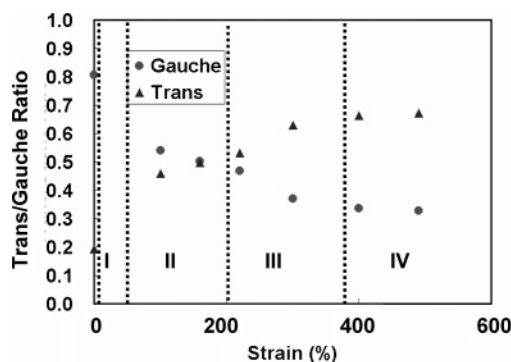


Figure 10. Change of *gauche* and *trans* fractions during uniaxial deformation by Raman spectroscopy.

The nature of the smectic phase can be characterized by the change of d spacing for the (001') reflection, which is shown in Figure 9. It is found that in zone II the d spacing of (001') reflection remains about constant (1.06 nm) at applied strains less than 130%, but it increases rapidly to 1.065 nm afterward. The range of the observed d spacings in zone II is always less than 1.075 nm, which is the length of the c -axis in the triclinic unit cell.⁵² In addition, the onset of the d spacing increase coincides with the rise of the applied load. These results imply the transformation from an oriented smectic C structure¹³ to an oriented smectic A-like structure (we termed this quasi-smectic A or q-A in order to be in accord with the published notion of the smectic A phase in PET^{7–12}) induced by stress, since the tilt angle in the smectic phase is decreased to a minimum value. The 1.06 nm d spacing observed in the early stage of zone II indicates that the molecular tilting angle in the smectic layer is approximately 9.6°; the 1.065 nm d spacing indicates that the molecular tilt angle in the smectic layer is approximately 7.8°. It is conceivable that the mechanical energy of uniaxial deformation (applies stress) of sample was consumed to extend the molecules in the smectic layer.

Figures 10 and 11 represent the changes of *gauche* and *trans* fractions of the ethylene glycol (EG) fragment (either in the isotropic slush, oriented slush, oriented smectic phase, or oriented crystalline regions) as well as the orientation of *gauche*, *trans* conformers and benzene ring of PET chains during uniaxial deformation, respectively. In Figure 10, it is seen that in zones I and II the overall *gauche* fraction of the EG fragment rapidly decreases (80% to 54%) while the overall *trans* fraction of the EG fragment increases (20% to 46%). Overall, these results are very similar to the recent

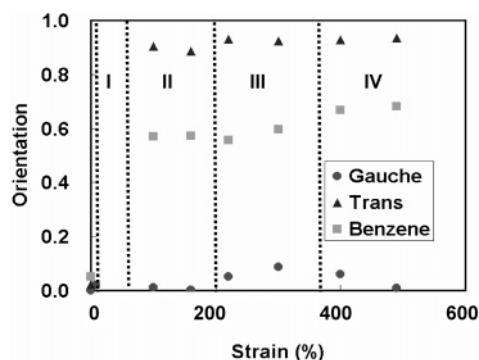


Figure 11. Change of orientation of *gauche*, *trans* and benzene ring during uniaxial deformation by Raman spectroscopy.

studies by Rodriguez-Cabello et al.,^{25,26} who used the Fourier transform Raman technique to follow the in-situ structural change (*trans/gauche* conformation ratio) of bulk PET under uniaxial deformation at different temperatures (room temperature up to 170 °C) as well as the study by Shen et al.,²⁹ who investigated the structural change of PET film by FT-IR during uniaxial deformation (at 67 and 88 °C), respectively. Shen et al. additionally observed that the population of *trans* conformer decreased in the preyielding region and then increased continuously after yielding at 67 °C. Unfortunately, we did not have enough experimental data to identify the behavior in the preyielding region (at zone I). On the basis of the combined WAXD and Raman results, we conclude that the majority of the *gauche* to *trans* conformational changes (in the C–C bond of the ethylene glycol fragments) occurs during the strain-induced isotropic slush to oriented slush transition, where no crystallization takes place.

In zone I, the orientations of both *trans*-EG fragment and benzene ring are found to increase dramatically (in Figure 11), while the orientation of the *gauche* fragment is quite negligible; where in zone II, the orientations of these three fragments remain about constant. These results are again consistent with our conclusion on the isotropic slush to oriented slush transformation in zone I. Thus, the oriented slush primarily consist of oriented benzene rings and *trans*-EG fragments, whereas the remaining isotropic phase mainly contains *gauche*-EG fragments with a low degree of orientation.

3.5. Zone III: Transition from Smectic to Triclinic Crystalline Phase and Formation of Lamellar Structure in Fibrils. In Figure 4, the triclinic crystalline structure with characteristic WAXD reflections was found to occur in zone III, where the oriented fraction increased and the unoriented fraction decreased with strain (Figure 7). Despite the apparent changes between the fractions of isotropic slush and oriented slush, we do not believe that the crystallization process occurs as a result of direct isotropic–crystalline transition. Instead, we suggest that the crystallization process takes place as a result of the smectic–crystalline transition, while events of transformations from isotropic slush-oriented slush and smectic C-quasi smectic A phases as well as transition between nematic–smectic phases also occur simultaneously. This conclusion was derived on the basis of the observations of abrupt changes in mass fraction and in *d* spacing of the smectic phase (Figures 8 and 9) upon the formation of crystalline phase. For example, in Figure 8, the rapid decrease in the mass fraction smectic phase in zone III is

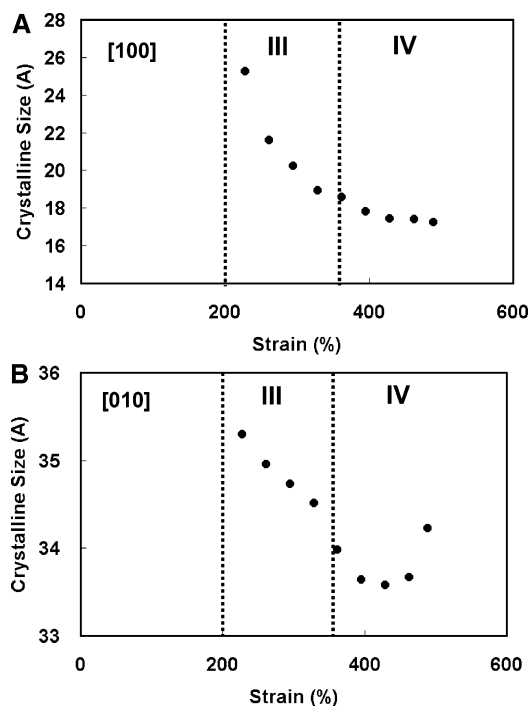


Figure 12. Changes of crystalline sizes using the Scherrer equation during uniaxial deformation. Data extracted from (A) (100) reflection and (B) (010) reflection in WAXD.

consistent with the smectic–crystalline transition. This indicates that the smectic phase is the precursor phase for crystallization, which has been recently pointed out by several groups.^{7,13,14}

We speculate that the structure transition between the smectic and crystalline phases may follow the following pathway. As the smectic C chains become elongated and aligned along the stretching direction (forming a quasi-smectic A structure), benzene molecules can slide, which may initiate the crystallization process. This hypothesis was based on our recent observation during uniaxial deformation of amorphous PET above its T_g (90 °C) using synchrotron WAXD.¹⁵ Results from this study indicated that the benzene molecules stacked more orthogonal to each other at the initial stage of crystal formation. With the increase in strain, the benzene molecules could slip past each other due to the shearing motion and eventually settled into a stable triclinic structure.^{15,16} In contrast, vertical stacking of benzene ring is quite unstable energetically, and this may be the reason why benzene rings slide relative to each other in triclinic unit cell. It is conceivable that a quasi smectic A structure may have such instability, and enthalpic stabilization such as displacement of benzene ring may be the driving force for the sliding motion, which induces the phase transition. The abrupt decrease in the *d* spacing of the (001') reflection in the smectic phase at the onset of crystallization is another interesting phenomenon. It is conceivable that the crystallization process probably alleviates a great deal of local stress in the strained smectic phase surrounding the crystalline domains, which converts the remaining “quasi-smectic A (q-A)” structure back to the stable smectic C structure. (The total mass fraction of the smectic phase is decreased because of the smectic–crystal transition.)

The crystallization process can be followed by monitoring the changes of crystalline reflections in WAXD. Figures 12 and 13 illustrate the changes in crystalline

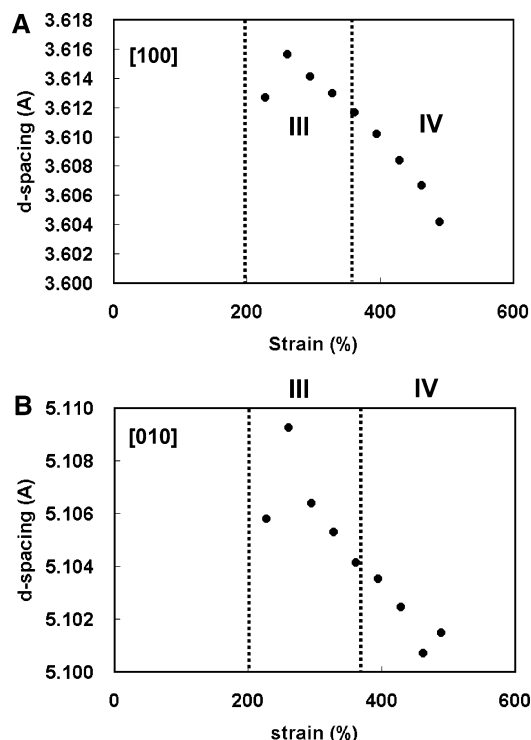


Figure 13. Changes of d spacing during uniaxial deformation. Data extracted from (A) (100) reflection and (B) (010) reflection in WAXD.

size and in d spacing of (100) and (010) reflections, respectively. It is seen that both crystalline sizes (based on (100) and (010) reflections) decrease with strain in zone III. There are two possibilities for this behavior: (1) the initial crystals are broken down by the increase in strain, or (2) the subsequently formed crystals are with smaller sizes. Judging by the results in Figure 13, where the d spacings of both (100) and (010) reflections are also found to decrease with strain, i.e., the crystalline structure becomes more perfect, we conclude that the latter (2) possibility is more likely. This suggests that the initially formed crystals are in larger sizes (although the crystalline perfection is lower), whereas the crystals formed at a later stage are smaller in size due to the volume constraint. The process of crystal perfection is probably a function of annealing time instead of a function of strain. In Figure 12, it is found that the crystalline size associated with the (010) reflection is larger than that of the (100) reflection, which is consistent with our earlier reports showing the preferred arrangement of benzene sheet structure in PET during strain-induced crystallization.^{15,16}

Raman results show the continuous conversion from *gauche* to *trans* conformation (Figure 10) in zone III. We believe that such changes are probably due to the continuous transformation from isotropic slush to oriented slush, induced by strain, instead of the smectic-crystalline transition (Figure 7). In Figure 11, it is interesting to note that the orientations of *gauche*, *trans* and benzene ring fragments all increase with strain in zone III. This observation is consistent with the notion that the formation of crystallites, even they are relatively imperfect, produces an effective three-dimensional network which significantly enhances the molecular orientation of all phases and thus the mechanical properties. (The applied load-strain curve appears to be linear with a positive slope.)

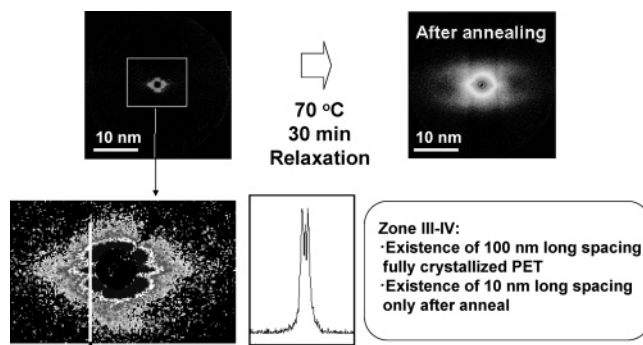


Figure 14. SAXS diagram collected at 400% strain (left) showing a long period of 100 nm. SAXS diagram of a fully crystallized PET sample (annealed at 70 °C for 30 min at a relaxed state) (right) showing a typical long period of about 100 nm.

The corresponding SAXS images collected in zone III exhibit extra scattering features on the meridian (Figure 6). The meridional scattering, showing a maximum value that corresponds to a long spacing around 100 nm, reflects the emergence of a very loosely arranged layered lamellar structure. The observed scattering maximum is quite different from the typical SAXS peak observed in fully crystallized PET samples, which usually exhibits a long period of lamellar structure around 10 nm. The SAXS patterns collected at 70 °C during deformation and from a fully crystallized PET sample—annealed at 70 °C for 30 min at the relaxation state—are shown in Figure 14. It is seen that the maximum scattering in SAXS during deformation is near the beam stop (or the resolution of our SAXS instrument), but the scattering pattern has sufficient scattering contrast. As the appearance of the meridional scattering maximum in SAXS coincides with the event of crystallization in WAXD, we conclude that crystallization generates a loosely arranged layered structure, probably within the fibrillar superstructure based on the persistent feature of the equatorial streak in SAXS. It is interesting to note that this 100 nm long spacing remains about constant during the deformation process in zones III and IV, which indicates the persistence of the lamellar layered structure.

3.6. Zone IV: Stabilization of Crystal Structure and Morphology. The structure, morphology, and property relationship in zone IV during deformation of PET, perhaps, has been most studied and best understood. It is evident that as strain-induced crystallization proceeds beyond a critical point (at the end of zone III), the strain-induced crystallites become perfected and grow into a stable network of lamellae, which can further advance the development of crystallites and the promotion of chain orientation. However, the process of crystallization in zone IV seems to be at a relatively slower rate, which is seen in the slower changes of crystalline sizes for both (100) and (010) reflections (Figure 12) as well as of *gauche*–*trans* transition and orientation of the *gauche*, *trans* and benzene ring fragments (Figures 10 and 11). Nevertheless, the process of crystalline perfection is found to take place continuously, which is seen by reductions in d spacings of (100) and (010) reflections (Figure 13). It is conceivable that the crystal perfection process is due to the annealing effect (at 70 °C) rather than the strain effect.

One interesting behavior in zone IV is the persistent appearance of scattering feature in SAXS patterns,

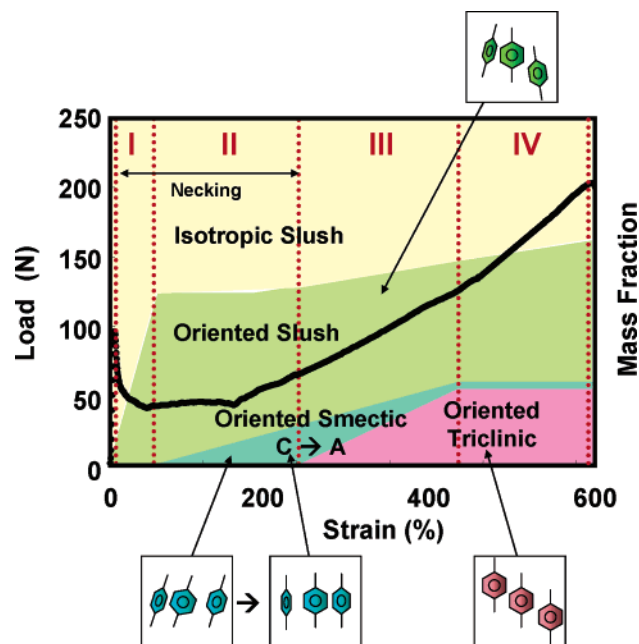


Figure 15. Strain-induced "phase" diagram of PET during deformation at 70 °C.

indicating the existences of a fibrillar superstructure as well as a loosely stacked crystalline lamellar structure (with a long period around 100 nm). On the basis of combined results from WAXD, SAXS, and Raman, we propose that the layered structure is formed within the fibril superstructure. As the length of the fibril is around several hundred nanometers, only several layers of crystalline lamellae are formed in the fibril, where the average width of the crystal layer is about several nanometers (as in Figure 12).

3.7. Strain-Induced Phase Transitions and Hierarchical Structural Development Pathways. The strain-induced phase transition "diagram" for a quenched PET sample during deformation at 70 °C is given in Figure 15. We note that this diagram is explained from a "dynamic" perspective rather than from a thermodynamic perspective. The mass fraction of each phase (the fraction unit was not given in Figure 15 because the estimate of the smectic phase was not precise, but the total fraction was 1) was derived from the WAXD data, which would change depending on the temperature and deformation rate. (The effect of deformation rate will be discussed elsewhere.) In Figure 15, contrary to the classical concept of strain-induced isotropic-crystal transition in PET, we argue that two phase transformations (isotropic slush-oriented slush and smectic C-quasi-smectic A) and two phase transitions (nematic-smectic and smectic-crystal) occur sequentially. It is interesting to see that the fraction of oriented slush is the largest throughout the deformation, and multiple phases (amorphous, nematic, smectic, and crystalline) coexist at high strains. The strain-induced oriented slush is probably dominated by presence of the oriented nematic phase, which preexists in the initial quenched sample.

Using data from Figure 15 as well as results from SAXS/Raman, we propose the following hierarchical structural development pathways and its relationship with the phase transformation and transition. The schematic diagrams for the pathways in different zones (I, II, and III) are illustrated in Figure 16A–C, respectively. The representative SAXS/WAXD patterns with

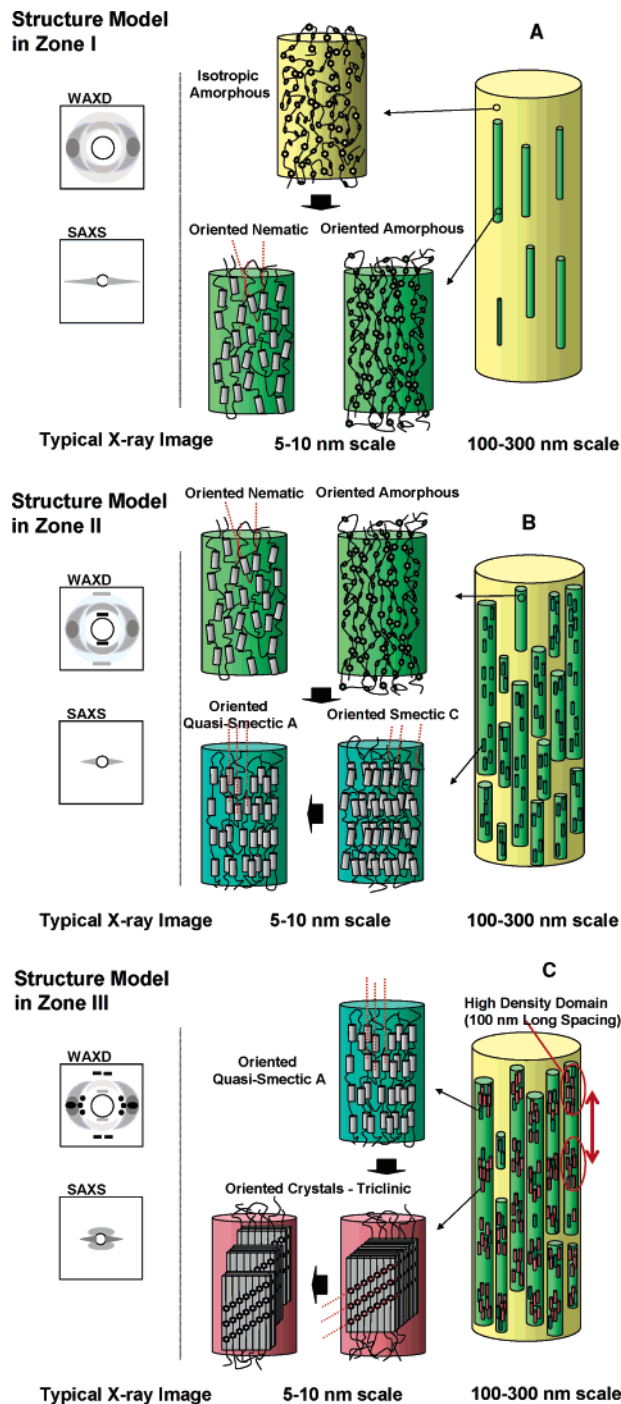


Figure 16. Schematic diagrams of phase transition and structure development pathways as well as corresponding SAXS/WAXD patterns during PET deformation at 70 °C in (A) zone I, (B) zone II, and (C) zone III (drawing not to scale). The cylinder in the nematic and smectic phases represents the mesogenic unit in PET with an aspect ratio of 2.

major scattering/diffraction features are also included in these diagrams. The major events in each zone during deformation are summarized below.

Zone I. We assume that the initial sample consists of isotropic slush with both amorphous and nematic components. Upon deformation, some isotropic amorphous chains are bound to be stretched, forming oriented amorphous phase; some unoriented nematic phase will be aligned, forming oriented nematic phase. The distinction between the oriented amorphous phase and the oriented nematic phase of PET chains having

marginal mesogenic unit will be very small, even though they differ each other from the range of ordering. The aggregation of oriented amorphous and oriented nematic phases seems to be in a corporative manner, resulting in a fibrillar-like superstructure (the length of the fibril is several hundred nanometers) at high strains. The yield point of the load–strain curve coincides with the first detection of the isotropic slush to oriented slush transformation. At the end of zone I, the oriented slush becomes the dominant component in the sample (its mass fraction is over 50%), while the applied load reaches a low plateau level.

Zone II. Within the fibrillar superstructure, the oriented slush–smectic C transition is observed. The formation of the smectic phase becomes the precursor for stress-induced crystallization. As the density contrast between the oriented slush and the smectic phase is low, no meridional scattering feature in SAXS is seen. During the “plastic deformation” stage, the oriented slush–smectic transition is detected, which can be attributed to the annealing process at 70 °C under tension. With the increase in strain, the tilt angle of the smectic C layer decreases, forming a structure similar to the quasi-smectic A phase. The transformation between the smectic C to quasi-smectic A phase appears to increase the applied load, marking the stage of strain hardening.

Zone III. Triclinic crystalline phase is formed from the strained quasi-smectic A phase by chain sliding. The formation of triclinic crystalline phase in the fibrillar superstructure leads to a crystalline lamellar structure with a long period of about 100 nm. SAXS can detect the lamellar structure because of the improved density contrast between the oriented crystalline phase and the surrounding oriented slush. Upon the formation of crystalline phase, the remaining smectic phase converts back into the stable smectic C structure, probably due to the relaxation of local stresses. The initial structure of the crystalline phase is relatively imperfect, which is dominated by the preferred arrangement of benzene sheet formation. The network of the imperfect crystallites enhances the mechanical properties and generates a near linear load–strain relationship.

4. Conclusion

The relationships between phase transition and hierarchical structural formation during uniaxial stretching of an amorphous PET sample were studied by means of in-situ WAXD, SAXS, and Raman techniques. A series of strain-induced phase transformations/transitions were observed by WAXD, including isotropic slush (i.e., the mixture of amorphous and nematic phases) to oriented slush, oriented slush to smectic C, smectic C to quasi-smectic A, and quasi-smectic A to triclinic crystalline phases, each can be used to characterize a unique stage of structure development during deformation of PET at 70 °C (zones I–III). The corresponding mechanical performance has a strong relationship with these phase transformation and transition processes. For example, the yield point is related to the onset of the isotropic slush to oriented slush transformation, the “plastic deformation” zone is related to the transformation of oriented mesophase, the onset of the stress increase is related to the smectic C-quasi-smectic A transformation, and the strain-hardening process is dominated by the smectic–triclinic crystalline transition. SAXS results indicate the formation of the fibrillar

superstructure is largely due to the transformation of isotropic slush to oriented slush without a true phase transition. A loosely stacked lamellar structure with a long period of 100 nm occurs within the fibrillar structure, probably initiated by the oriented slush–smectic transition, but only become visible (by SAXS) after the smectic–crystalline transition. A strain-induced “phase” transition diagram and the possible pathways for the hierarchical structural development during deformation have been proposed in this study.

Acknowledgment. The authors thank the financial support from National Science Foundation (DMR-0405432), the National Textile Center, and the Toray Industry in Japan. The authors also thank Mr. Uchida from Toray for the synthesis of experimental PET samples and Dr. Dufei Fang for the assistance of the image analysis.

References and Notes

- (1) Bates, M. A.; Frenkel, D. *J. Chem. Phys.* **2000**, *112*, 10034.
- (2) Imai, M.; Kaji, K.; Kanaya, T.; Sakai, Y. *Phys. Rev. B* **1995**, *52*, 12696.
- (3) Bonart von, R. *Kolloid-Z.* **1966**, *213*, 1.
- (4) Bonart von, R. *Kolloid Z. Z. Polym* **1968**, *231*, 16.
- (5) Welsh, G. E.; Blundell, D. J.; Windle, A. H. *Macromolecules* **1998**, *31*, 7562.
- (6) Welsh, G. E.; Blundell, D. J.; Windle, A. H. *J. Mater. Sci.* **2000**, *35*, 5225.
- (7) Asano, T.; Balta-Calleja, F. J.; Flores, A.; Tanigaki, M.; Mina, M. F.; Sawatari, C.; Itagaki, H.; Takahashi, H.; Hatta, I. *Polymer* **1999**, *40*, 6475.
- (8) Blundell, D. J.; Mahendrasingam, A.; Martin, C.; Fuller, W. *J. Mater. Sci.* **2000**, *35*, 5057.
- (9) Mahendrasingam, A.; Blundell, D. J.; Martin, C.; Fuller, W.; MacKerron, D. H.; Harvie, J. L.; Oldman, R. J.; Riekel, C. *Polymer* **2000**, *41*, 7803.
- (10) Blundell, D. J.; Mahendrasingam, A.; Martin, C.; Fuller, W.; MacKerron, D. H.; Harvie, J. L.; Oldman, R. J.; Riekel, C. *Polymer* **2000**, *41*, 7793.
- (11) Mahendrasingam, A.; Martin, C.; Fuller, W.; Blundell, D. J.; Oldman, R. J.; MacKerron, D. H.; Harvie, J. L.; Riekel, C. *Polymer* **2000**, *41*, 1217.
- (12) Blundell, D. J.; MacKerron, D. H.; Fuller, W.; Mahendrasingam, A.; Martin, C.; Oldman, R. J.; Rule, R. J.; Riekel, C. *Polymer* **1996**, *37*, 3303.
- (13) Ran, S.; Wang, Z.; Burger, C.; Chu, B.; Hsiao, B. S. *Macromolecules* **2002**, *35*, 10102.
- (14) Mahendrasingam, A.; Blundell, D. J.; Wright, A. K.; Urban, V.; Narayanan, T.; Fuller, W. *Polymer* **2003**, *44*, 5915.
- (15) Kawakami, D.; Ran, S.; Burger, C.; Fu, B.; Sics, I.; Hsiao, B. S. *Macromolecules* **2003**, *36*, 9275.
- (16) Kawakami, D.; Ran, S.; Burger, C.; Fu, B.; Sics, I.; Hsiao, B. S.; Kikutani, T. *Polymer* **2004**, *45*, 905.
- (17) Crist, B. *Mater. Sci. Technol.* **1993**, *12*.
- (18) Chu, B.; Hsiao, B. S. *Chem. Rev.* **2001**, *101*, 1727.
- (19) Fraser, R. D. B.; Macrae, T. P.; Miller, A.; Rowlands, R. J. *J. Appl. Crystallogr.* **1976**, *9*, 81.
- (20) Klug, H. P.; Alexander, L. E. *X-ray Diffraction Procedures*; John Wiley & Sons: New York, 1954.
- (21) Salem, D. R. *Polymer* **1992**, *33*, 3182.
- (22) Salem, D. R. *Polymer* **1992**, *33*, 3189.
- (23) Natarajan, S.; Michielsen, S. *J. Appl. Polym. Sci.* **1999**, *73*, 94, 3.
- (24) Yang, S.; Michielsen, S. *Macromolecules* **2002**, *35*, 10108.
- (25) Yang, S.; Michielsen, S. *Macromolecules* **2003**, *36*, 6484.
- (26) Rodriguez-Cabello, J. C.; Merino, J. C.; Fernandez, M. R.; Pastor, J. M. *J. Raman Spectrosc.* **1996**, *27*, 23.
- (27) Rodriguez-Cabello, J. C.; Merino, J. C.; Quintanilla, L.; Pastor, J. M. *J. Appl. Polym. Sci.* **1996**, *62*, 1953.
- (28) Middleton, A. C.; Ducketti, R. A.; Ward, I. M.; Mahendrasingam, A.; Martin, C. *J. Appl. Polym. Sci.* **2001**, *79*, 1825.
- (29) Shen, D.; Long, F.; Wen, Z.; Qian, R. *Makromol. Chem.* **1991**, *192*, 301.
- (30) Siesler, H. W. *Adv. Polym. Sci.* **1984**, *21*, 55.
- (31) Gupta, V. B.; Ramesh, L.; Siesler, H. W. *J. Polym. Sci., Polym. Phys. Ed.* **1985**, *23*, 405.
- (32) Siesler, H. W. *Pure Appl. Chem.* **1985**, *57*, 1603.

- (33) Lesco, C. C. C.; Rabolt, J. F.; Ikeda, R. M.; Chase, B.; Kennedy, A. *J. Mol. Struct.* **2000**, 521, 127.
- (34) Lee, S.; Miyaji, H.; Geil, P. H. *J. Macromol. Sci., Phys.* **1983**, B22, 489.
- (35) Fukao, K.; Koyama, A.; Tahara, D.; Kozono, Y.; Miyamoto, Y.; Tsurutani, N. *J. Macromol. Sci., Part B* **2003**, B42, 717.
- (36) Yeh, G. S. Y.; Geil, P. H. *J. Macromol. Sci., Part B* **1967**, 1, 235.
- (37) Yeh, G. S. Y.; Geil, P. H. *J. Macromol. Sci., Part B* **1967**, 1, 251.
- (38) Taiko, H.; Chagin, T.; Kawakami, D.; Goddard, W. A., III *Polym. Prepr.* **2004**, 45, 794.
- (39) Kimura, T.; Kawai, T.; Sakamoto, Y. *Polymer* **2000**, 41, 809.
- (40) Brown, H. R.; Kramer, E. J. *J. Macromol. Sci., Phys.* **1981**, B19, 487.
- (41) Brown, H. R.; Mills, P. J.; Kramer, E. J. *J. Polym. Sci., Polym. Phys.* **1985**, 23, 1857.
- (42) Grubb, D. T.; Prasad, K.; Adams, W. *Polymer* **1991**, 32, 1167.
- (43) Grubb, D. T.; Prasad, K. *Macromolecules* **1992**, 25, 4575.
- (44) Ran, S.; Fang, D.; Zong, X.; Hsiao, B. S.; Chu, B.; Cuniff, P. M. *Polymer* **2001**, 42, 1601.
- (45) Ran, S. F.; Zong, X. H.; Fang, D. F.; Hsiao, B. S.; Chu, B.; Cuniff, P. M.; Phillips, R. A. *J. Mater. Sci.* **2001**, 36, 3071.
- (46) Hsiao, B. S.; Kennedy, A. D.; Leach, R. A.; Chu, B.; Harney, P. *J. Appl. Crystallogr.* **1997**, 30, 1084.
- (47) Somani, R. H.; Yang, L.; Sics, I.; Hsiao, B. S.; Pogodina, N. V.; Winter, H. H.; Agarwal, P.; Fruitwala, H.; Tsou, A. *Macromol. Symp.* **2002**, 185, 105.
- (48) Somani, R. H.; Yang, L.; Hsiao, B. S.; Agarwal, P. K.; Fruitwala, H. A.; Tsou, A. H. *Macromolecules* **2002**, 35, 9096.
- (49) Mendelson, A. *Plasticity: Theory and Application*; Kreiger: Huntington, NY, 1983.
- (50) Lubliner, J. *Plasticity Theory*; Prentice-Hall: Upper Saddle River, NJ, 1998.
- (51) Hill, R. *Mathematical Theory of Plasticity*; Oxford University Press: New York, 1998.
- (52) Daubery, R. D.; Bunn, C. W.; Brown, C. J. *Proc. R. Soc. London A* **1954**, 226, 531.

MA049333X